An MRI Compatible RF MEMs Controlled Wireless Power Transfer System

Kelly Byron, *Student Member, IEEE*, Simone A. Winkler, *Senior Member, IEEE*, Fraser Robb, *Member, IEEE*, Shreyas Vasanawala, John Pauly, *Member, IEEE*, and Greig Scott, *Member, IEEE*

***Abstract*— In magnetic resonance imaging (MRI), wearable wireless receive coil arrays are a key technology goal. An MRI compatible wireless power transfer (WPT) system will be needed to realize this technology. An MRI WPT system must withstand the extreme electromagnetic environment of the scanner and cannot degrade MRI image quality. Here, a WPT system is developed for operation in MRI scanners using new microelectromechanical RF (RF MEMs) switch technology. The WPT system includes a class-E power amplifier, RF MEMs automated impedance matching, a primary coil array employing RF MEMs power steering, and a flexible secondary coil with class-E rectification. To adapt WPT technology to MRI, techniques are developed for operation at high magnetic field, and to mitigate the RF interactions between the scanner and WPT system. A major challenge was the identification and suppression of noise and harmonic interference, by gating, filtering, and rectifier topologies. The system can achieve 63% efficiency while exceeding 13-W delivery over a coil distance of 3.5 cm. For continuous WPT beyond 5 W, added filters and full-wave class-E rectification lower harmonic generation at some cost to efficiency, while image signal-to-noise ratio (SNR) reaches about 32% of the ideal. RF-gated WPT, which interrupts power transfer in the MRI signal acquisition interval, achieves SNR performance to within 1 dB of the ideal. With further refinement, the inclusion of WPT technology in MRI scanners appears completely feasible.**

***Index Terms*— Impedance matching, microelectromechanical (MEMs) systems, wireless power transfer (WPT).**

I. Introduction

WIRELESSLY powered medical devices present unique challenges for wireless power transfer (WPT) systems. Power levels and device dimensions are often restricted while demanding increased robustness for dynamic environments. In magnetic resonance imaging (MRI), there is the added challenge of a large, 1.5–3 T, static magnetic field, pulsed high-amplitude gradient coil fields, high-power (10–30 kW) RF transmit pulses, and the resulting detection of nuclear spin precession near the thermal noise floor after excitation by the RF pulse. The nuclear magnetic resonance signal from the patient is detected by nearby MRI receive coils for reconstruction of the MR image. The signal-to-noise ratio (SNR) of these images can be improved with larger arrays of smaller MRI receive coils placed directly on the patient. The trend toward high channel counts has engendered efforts to make coil arrays lighter and less rigid for patient comfort. Flexible coils can further improve SNR by virtue of better anatomical conformity [1]–[3]. For conformable receive arrays, the weight reduction and flexibility have been limited by bulky connectors, baluns, and external cabling. This has led to the goal of making completely wireless and wearable coil arrays powered by WPT technology.

To support 100–300 mW per MRI receive channel, a WPT system must be capable of delivering 3–10 W for a 32 channel system. Some basic components of this system are presented in [4], including a flexible WPT secondary coil and rectifier components that could be integrated with wearable, conformal MRI coil arrays. We propose the concept of an array of WPT primary coils embedded in an MRI patient table, as shown in Fig. 1. A flexible secondary coil can be wrapped around the back of the patient to minimize the distance between WPT coils. To operate proximal to the MRI bore, all key WPT components must be immune to static and pulsed field influence, and appear transparent to the MRI system operation.

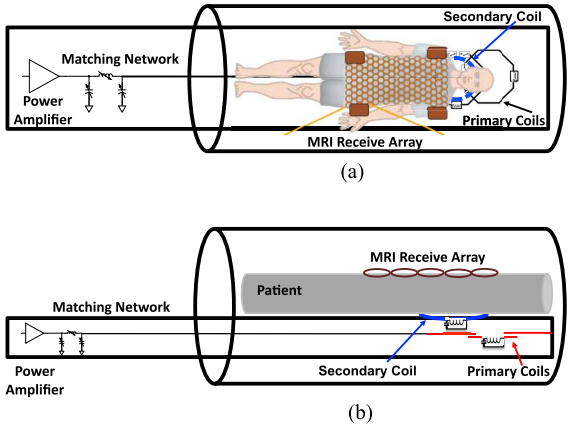

Fig. 1. WPT system embedded in an MRI and powering an MRI receive coil array. (a) Top view. (b) Side view.

Manuscript received August 31, 2018; revised December 31, 2018; accepted February 8, 2019. This work was supported in part by the National Institutes of Health under Grant R01EB019241 and in part by GE Healthcare. This paper is an expanded version from the IEEE Wireless Power Transfer Conference, Montreal, QC, Canada, June 3–7, 2018. *(Corresponding author: Kelly Byron.)*

K. Byron is with the Department of Electrical and Computer Engineering, Stanford University, Stanford, CA 94305 USA (e-mail: kbyron@stanford.edu).

S. A. Winkler and S. Vasanawala are with the Department of Radiology, Stanford University, Stanford, CA 94305 USA.

F. Robb is with GE Healthcare, Aurora, OH 44202 USA.

J. Pauly and G. Scott are with the Department of Electrical and Computer Engineering, Stanford University, Stanford, CA 94305 USA.

Color versions of one or more of the figures in this paper are available online at http://ieeexplore.ieee.org.

Digital Object Identifier 10.1109/TMTT.2019.2902554

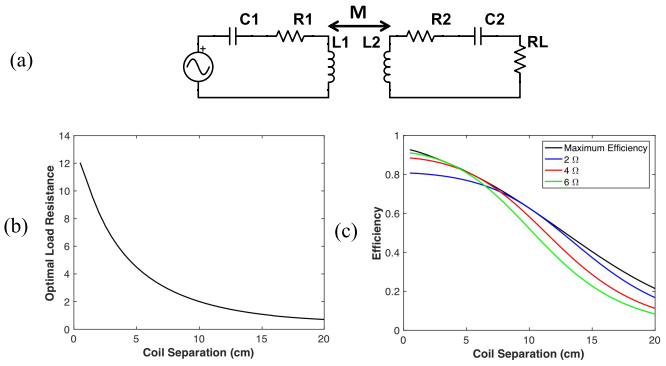

Fig. 2. WPT. (a) Basic coupled coil circuit model. (b) Optimal load resistance variation with increasing distance between coils. (c) Calculated efficiency variation with increasing distance between coils for different load resistances. Plots use later experimental results of R1 = 0.89Ω, R2 = 0.46Ω, a 20-cm primary and 18-cm secondary.

In this paper, we present and extend a complete WPT prototype for operation in MRI by employing next-generation nonmagnetic microelectromechanical RF (RF MEMs) switch technology. The WPT system includes a class-E power amplifier, RF MEMs automated impedance matching, a primary coil array employing RF MEMs power steering, and a flexible secondary coil with class-E rectification. To adapt WPT technology to the MRI bore, techniques are developed for operation at high magnetic field, and to mitigate the RF interactions between the scanner and WPT system. Only direct current (dc) supply lines need to be routed outside the scan room. A major challenge, the identification and suppression of noise and harmonic interference, is addressed by gating, filtering, and rectifier topology methods. The system can achieve 63% efficiency while exceeding 13-W delivery to a 4-Ω load over a coil distance of 3.5 cm. For continuous WPT beyond 5 W, added filters and full-wave class-E rectification lower harmonic generation at some cost to efficiency. In this case, image SNR reaches about 32% of the ideal for 8.6-W power delivery at 33% efficiency. Alternately, RF-gated WPT, which interrupts power transfer in the MRI signal acquisition interval, achieves SNR performance within 87%–95% of the ideal. The following sections outline the key WPT adaptations and novel use of RF MEMs for our MRI WPT prototype.

II. Wireless Power Transfer Efficiency

In resonant inductively coupled WPT systems, a primary coil generates a magnetic field that induces current on a nearby secondary coil, thereby transferring power. Fig. 2(a) shows an equivalent circuit model for two resonant coupled coils. The WPT inductive link acts as a loosely coupled transformer and can be modeled by a two-port network [5], [6].

The coupling between coils causes the secondary coil to induce a series load impedance on the primary coil. Series capacitors resonate the coils at the frequency of power transfer, ideally impressing a purely real impedance $R_{\rm eq}$ on the primary, dependent on the mutual inductance M between coils, the parasitic loss R_2 of the secondary coil, and the load resistance R_L, with the result

$$R_{\rm eq} = \frac{\omega^2 M^2}{R_2 + R_L}. \tag{1}$$

The mutual inductance, which depends on coil radii and separation, can be calculated using Neumann's formula [7] by integrating around the coil contours C_1, C_2 as

$$M = \frac{\mu_0}{4\pi} \iint_{C_1 C_2} \frac{{\rm d}s_1 \cdot {\rm d}s_2}{|R_{12}|}. \tag{2}$$

$R_{\rm eq}$ forms a resistive divider with the parasitic resistance of the primary coil, allowing for simple equations to determine the efficiency, $\eta_{\rm ps}$, from the primary to secondary and $\eta_{\rm sl}$ from the secondary coil to the load, which can be combined as

$$\eta_{\rm link} = \eta_{\rm ps} * \eta_{\rm sl} = \frac{R_{\rm eq}}{R_1 + R_{\rm eq}} * \frac{R_L}{R_2 + R_L} \tag{3}$$

$$= \frac{\omega^2 M^2 R_L}{\omega^2 M^2 (R_2 + R_L) + R_1 (R_2 + R_L)^2} \tag{4}$$

giving the efficiency of the WPT inductive link when the coils are perfectly resonant.

By following the derivation of [6], assigning the auxiliary parameter

$$X = \frac{\omega^2 M^2}{R_1 R_2} \tag{5}$$

in (4), and differentiating with respect to R_2, the maximum theoretical link efficiency $\eta_{\rm link,max}$ of the coupled coils simplifies to

$$\eta_{\rm link,max} = \frac{X}{(1 + \sqrt{1 + X})^2}. \tag{6}$$

To achieve this efficiency limit, the load resistance must be matched to the optimal load resistance of

$$R_{L,\rm opt} = R_2 \sqrt{1 + X}. \tag{7}$$

Optimal link efficiency is achieved by maximizing X, namely, maximizing the coupling between coils and minimizing the parasitic loss in the coils. The load for optimal efficiency differs from that of maximum power delivery. The latter is achieved if $R_L = R_2$, in which case the delivered load power is $X/4$ of the power dissipated in R_1, and link efficiencies must be below 50% [6].

The optimal load resistance and its variation with coil separation can be plotted for 10 MHz using (2) and *a priori* measured coil parameters, as shown in Fig. 2(b). Fig. 2(c) shows that if the load resistance is held constant, $\eta_{\rm link,max}$ will only be reached at a specific coil separation. For a distance of 3.5 cm, $\eta_{\rm link}$ is maximized with a load resistance of 6 Ω, but at larger distances, this load resistance drops rapidly from the maximum. As a result, our later efficiency measurements employ a 4-Ω load, which will provide a near-optimal load resistance for a wider range of coil distances.

The link efficiency ($\eta_{\rm link}$) takes into consideration only the coil losses and loading. The total system efficiency

$$\eta_{\rm system} = \eta_{\rm dc-RF} * \eta_{\rm match} * \eta_{\rm link} * \eta_{\rm RF-dc} \tag{8}$$

includes the efficiency of the power amplifier, matching network, and rectification. Implicit is the interaction between stages. Variations in coil positions or R_L can cause large

efficiency losses in other stages without adjustable matching. For example, if R_L represents the impedance looking into a dc–dc converter placed after the rectifier, R_L will vary with the voltage supplied to the converter. For this paper, we consider only a load resistor on the output of the rectifier, since a second matching network to an arbitrary passive load is possible. Future work will consider active loads.

III. System Design

A. Frequency Choice

WPT systems are typically categorized as near-field, mid field, and far-field, based on the distance and frequency of power transfer. In MRI, we are constrained to the central bore dimensions, but require lateral freedom of placement to collocate WPT coils with the MRI receive array, whose exact placement will vary with patient and scan table position. Midfield WPT, employing resonant inductive coupling (or colloquially, magnetic resonance), avoids ferrous components yet can deliver power levels exceeding 10 W. However, the ISM band at 6.78 MHz is unsuitable for continuous WPT in MRI. We previously chose 10 MHz [8], because harmonics generated by the WPT system at intervals of 10 MHz will bracket the MRI bands of both 1.5-T (64 MHz) and 3-T (128 MHz) scanners. A Crystek crystal oscillator is presently used, but 10 MHz conveniently allows synchronous locking to the scanner frequency reference. For RF-gated WPT, this constraint can be relaxed. Higher WPT frequencies create wider harmonic frequency gaps, but increase specific absorption rate (SAR) exposure for humans and degrade WPT efficiency, as patient losses increase approximately quadratically with frequency.

B. WPT Coils

To collocate the WPT secondary coil with the MRI coil array, we used an 18 cm diameter, flexible harvesting loop made of a single turn 18 AWG wire, as shown in Fig. 3(b). Ideally, the primary coil should be the same size to maximize the mutual inductance between coils, but in a practical system, it would be difficult to ensure that smaller coils are aligned. Consequently, we constructed three 20-cm-diameter primary coils, shown in Fig. 3(a), which can be individually switched to steer power through a preselected element. This maximizes coupling to the secondary coil over a large range of coil placements. The primary coils are 1-oz copper with tin finish printed on FR-4.062 in material with a trace width of 6.35 mm.

Neighboring coils, individually tuned to the same frequency, can induce cross coupling. If multiple coils couple to the selected primary, instead of an induced single peak impedance, frequency splitting will arise with multiple impedance peaks and shifts. To prevent this, adjacent coils can be optimally overlapped to null their mutual inductance [9], allowing an individual primary coil to predominantly couple with a single secondary coil. Two RF MEMS switches are placed in series with each primary coil to control in which array element transmits power. With a single switch, one side of the primary element and drive cable conductor can form a continuous parasitic antenna that creates indirect coupling and

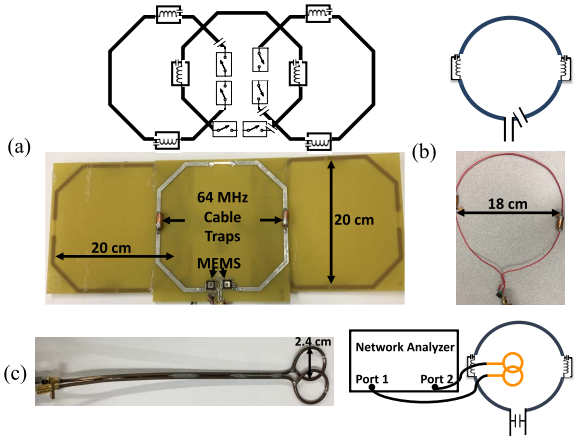

Fig. 3. WPT coil. (a) Array of primary coils with two RF MEMs switches, one on each side of the series-resonant coils and 64-MHz cable traps on each coil. (b) Single flexible secondary loop that is also series-resonant at 10 MHz with 64-MHz cable traps. (c) Decoupled pair of split-shielded loops for S21 measurement on network analyzer to extract coil quality factor.

crosstalk between separated MRI receive elements, degrading image SNR. Switches are placed on each side of the coil feed to fully disconnect common-mode cable coupling when the given drive loop is disabled.

The primary and secondary coils were all series-tuned to 10 MHz and included shielded *LC* cable traps at 64 MHz to further inhibit coupling to nearby MRI receive coils. Coil quality factor (Q) was measured by resonating with high-Q capacitors (NPO/C0G) in parallel. A decoupled pair of overlapped split-shielded loops (for zero direct S21) was placed above the resonant coil to sense the tuned response. The S21 between the sniffer loops was measured by network analyzer, with center frequency and 3-dB bandwidth extracted to calculate Q. For each primary coil (L1 = 620 nH), the unloaded Q was about 163 without the MEMS switches, and secondary coil Q was approximately 127 (R2 = 0.46 Ω with L2 = 930 nH). With the addition of the RF MEMS switches, the measured primary Q dropped to about 44 as a result of the approximate 0.4-Ω resistance of each RF MEMs switch when closed.

The impact of the primary MEMs switches can be assessed with the aid of the link efficiency equations. For a target coil separation of 3.5 cm (M ≈ 132.5 nH), and the measured coil parameters, the link efficiency (η_{link}) shown in Fig. 2 reaches 84.9% with a 4-Ω resistor load and primary coil Q of 44 (MEMs present). Without the MEMS switches, and primary Q of 163, η_{link} increases to 88.3%. If optimal loads were used (6.0 Ω and 11.6 Ω, respectively), the achievable link efficiencies go from 85.8% with a primary Q of 44%–92.3% with a Q of 163. Although the MEMs can decrease η_{link} by 4%–6%, R_{eq} tends to dominate these losses. By comparison, the transfer efficiency (η_{system}) would drop over 30% if a single large area primary of similar coverage area was used.

C. Class-E Power Amplifier

Class-E power amplifiers are commonly used in WPT systems for their high efficiency and simple design equations [10]–[13]. Theoretically, these amplifiers can

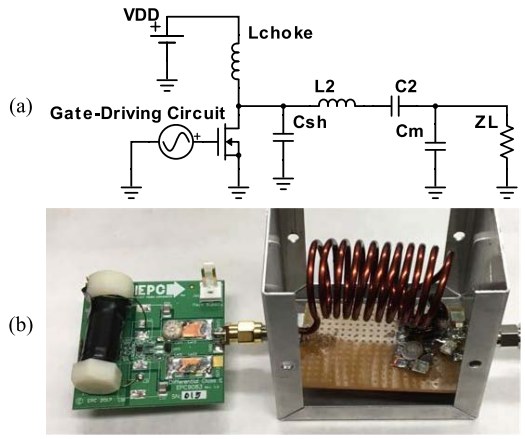

Fig. 4. Class-E power amplifier. (a) Circuit diagram. (b) Physical implementation employing EPC9083 eval board and filtering with high Q air-core inductors.

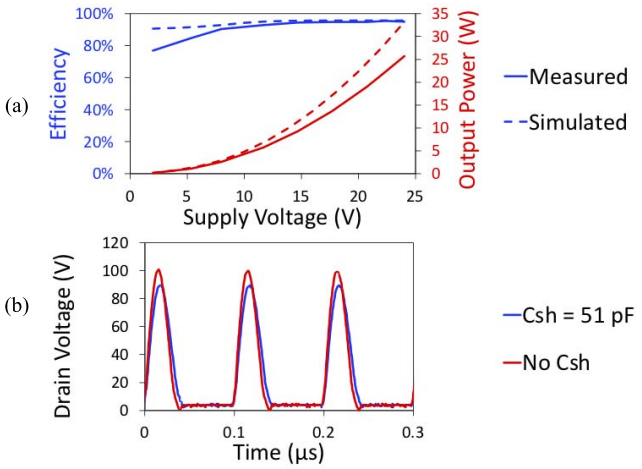

Fig. 5. (a) Power amplifier output power and efficiency for increasing dc supply voltages measured from benchtop tests and simulated in LTSpice with a finite Q L_2 and EPC2046 device model. (b) Measured voltage at the drain of the transistor with and without added capacitance in parallel with the transistor, demonstrating class-E operation.

approach 100% efficiency by operating the transistor as a switch while designing the load network to shape the amplifier waveforms to prevent simultaneous overlap of high voltage and high current in the transistor [14]–[16]. Fig. 4(a) shows the circuit model of our class-E power amplifier, which is based on Sokal's design equations given in [17].

The class-E amplifier employs the EPC9083 demo board, which includes the gate driver and an EPC2046 eGaN FET. An eGaN device minimizes the parasitic resistance and capacitance [18]–[20]. V_{DD} was chosen to be 24 V so that the nominal drain voltage of 3.56 $\times$ V_{DD} would be well below the transistor breakdown voltage of 200 V. The amplifier is designed to output 30 W and have a loaded Q of 5. This gives an optimal load resistance of 9.92 Ω. Because space is extremely limited inside the MRI bore, it is more practical to locate the power amplifier and autotuner at the front edge of the magnet, with 50-Ω coax connecting to the primary coil and an optional prematch at the bore center. As a result, to minimize cable losses, the power amplifier is matched to a 50-Ω characteristic impedance by using C_m to step down R_L from 50 to 9.92 Ω. This leads to an extra series capacitance that combines with L_2 and C_2 to form a resonant filter at the fundamental frequency.

Fig. 4(b) shows the physical implementation of this amplifier, where L_2 is physically large to minimize parasitic loss, achieving a measured Q of 193. The large L_2 value of 1.1 μH provides a sufficiently high Q when combined with the equivalent load resistance for the output voltage to be sinusoidal [17]. An air-core inductor is also used for L_{choke} (9 μH) to avoid saturation in the MRI magnetic field. The power amplifier is shielded to prevent radiation of noise and interference in the MRI environment.

The dc supply voltage to the power amplifier can be varied to transmit different power levels to the load. However, the efficiency of the power amplifier will now vary, as shown in Fig. 5(a), because of the device parasitic capacitance variation with voltage, effectively changing the required C_{sh} capacitance for optimal efficiency. For the desired V_{DD} of 24 V, the optimal C_{sh} was estimated to be 51 pF according to LTSpice simulations. These simulations included the finite Q of L_2 and EPC's eGaN device model, which estimates C_{DS} of the FET based on the device voltage. C_{sh} was verified on the lab bench by observing the drain voltage of the transistor. As shown in Fig. 5(b), an added capacitance of 51 pF generated the optimal drain voltage waveform—the voltage returns to zero exactly before the transistor turns on and the current begins to rise.

D. Sensitivity to Load Variation

The efficiency of a class-E power amplifier is highly dependent on the load impedance maintaining the constant resistive value of the design equations. This can be difficult to ensure in WPT systems, where the load impedance presented to the power amplifier is the impedance transformed R_{eq} of the coupled coils. As discussed in Section II, R_{eq} is highly dependent on the mutual inductance between the coils, which varies with relative coil position. From the testing of a few practical coil positions, $R_{\text{eq}}+R_1$ ranged from 3.44 to 19.5 Ω as shown in Fig. 6. The corresponding variation in link efficiency can be determined with (3). With a load resistance of 4 Ω, and coil Q derived R_1 of 0.89 Ω and R_2 of 0.46 Ω, link efficiency would decrease from 85.6% to 66.5% as R_{eq} decreases, resulting in a commensurate decrease in total system efficiency η_{system} of (8). Without autotuning, R_{eq} would also modulate the power amplifier load and efficiency ($\eta_{\text{dc-RF}}$), further degrading η_{system}. The nonlinear element used for rectification on the secondary may also add a reactive component to the load impedance. Additional cable lengths and proximity to the MRI bore shielding will further change the reactance seen by the power amplifier.

Fig. 7 shows the measured efficiency and delivered power variation when a manual antenna tuner (MFJ Enterprises MFJ-904H) is used to perform a simplified load–pull test. The manual tuner forms a pi-match with two air variable capacitors and a tapped inductor of three stacked powder iron toroids. The manual tuner was inserted between a 50-Ω 30-dB attenuator load and a network analyzer S11 input and adjusted to various complex impedance values, as shown

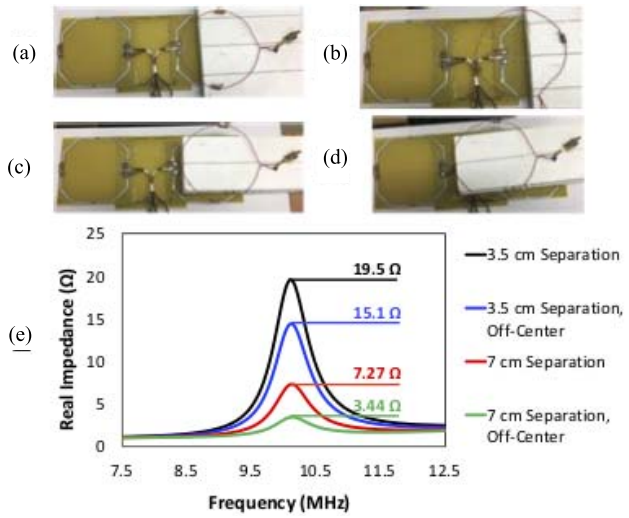

Fig. 6. Input impedance of a single primary coil with a coupled secondary coil connected to a 4-Ω resistor. (a) Centered 3.5 cm above the primary coil. (b) 3.5 cm above the primary coil and shifted off-center. (c) Centered 7 cm above the primary coil. (d) 7 cm above the primary coil and shifted off-center. (e) Resulting real impedance versus frequency at each position.

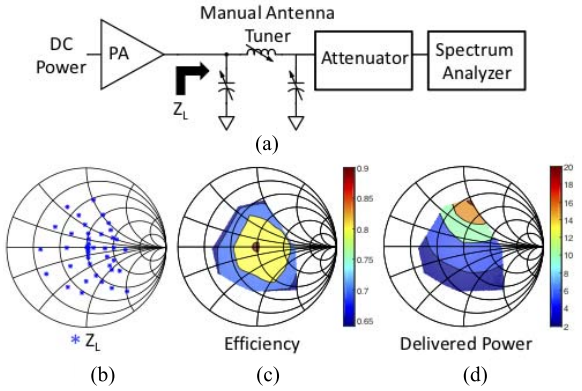

Fig. 7. Class-E power amplifier load–pull tests. (a) Test setup using a manual antenna tuner MFJ-904H to provide load–pull variation. (b) Selected load impedances at the power amplifier output. (c) Measured efficiency variation over the range of load impedances. (d) Measured power delivered for the load impedance range.

in Fig. 7(b). The attenuator output was then connected to a spectrum analyzer, while the input port provided the amplifier load impedance to measure power amplifier efficiency and delivered power. This approach is limited to synthesizing the impedance at the WPT frequency, adjustment of harmonic impedances was not possible.

The power amplifier maintains a high efficiency only for a narrow range of load impedances around 50 Ω. The delivered power also varies greatly with dc supply voltage, while inductive or capacitive loads will cause a respective increase or decrease in power delivered. This variation was confirmed in LTSpice simulations with the power amplifier. As a result, we designed an RF-MEMs controllable impedance matching network for the power amplifier output. This prevents the amplifier from seeing large resistance and reactance variations in load impedance that could be destructive at high power levels. Although there will be some insertion loss through the matching network, the overall improvement in

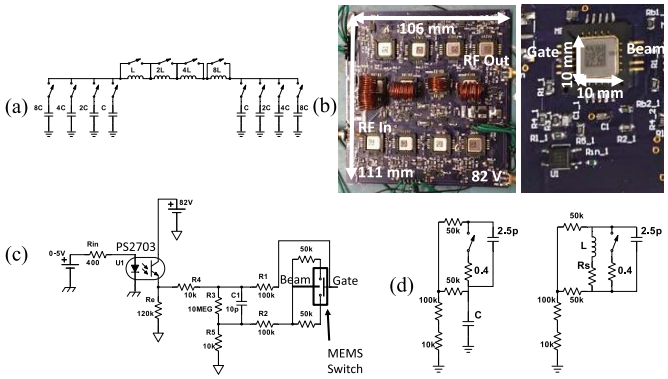

Fig. 8. Impedance matching network circuit (a) with 12 ideal switches, (b) complete board and close up of one of the MEMS switches, (c) gate driver for each MEMS switch, and (d) single switch with parasitics in series with a capacitor and in parallel with a lossy inductor.

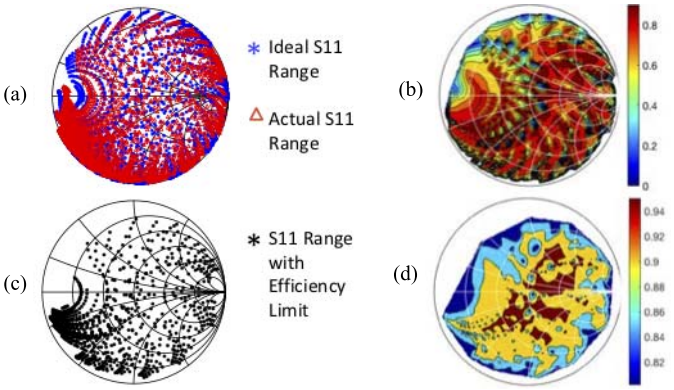

Fig. 9. Impedance matching network. (a) Ideal range of S11 load values (blue) and S11 load values including switch and board parasitics (red) that can be matched to 50 Ω. (b) Calculated efficiency through the matching network for each S11 value exactly matched to 50 Ω. (c) Range of S11 values that can be matched to 50 Ω with greater than 80% efficiency. (d) Calculated efficiency for the range of S11 values matched to 50 Ω that are used for tuning.

power amplifier efficiency should compensate for most load impedance values.

E. Controllable Impedance Matching System

The tunable matching network employs the pi-match circuit as shown in Fig. 8(a). Binary weighted capacitor and inductor values allow matching over an evenly distributed range of reflection coefficients to 50 Ω [21]. New generation RF MEMs devices, which performed switching of the matching network components, were chosen for their low parasitic capacitance and high-power capability. The RF MEMS (general Electric/ MenloMicro M7100) was designed specifically for operation in MRI applications [22], [23] to reconfigure the geometry of MRI coil arrays or replace the p-i-n diodes currently used for MR surface coil decoupling. This RF MEMS switch is nonmagnetic, with a specified nominal series resistance of 0.4 Ω, and high voltage (500 V) and current (greater than 5 A) capability.

Fig. 9(a) shows that with 12 ideal switches and $C_{\min}$ of 110 pF and $L_{\min}$ of 170 nH, almost the entire Smith chart can be covered (blue), even when measured parasitic losses on the board are considered (red). These losses include the resistors used in the gate driver circuitry for the switches,

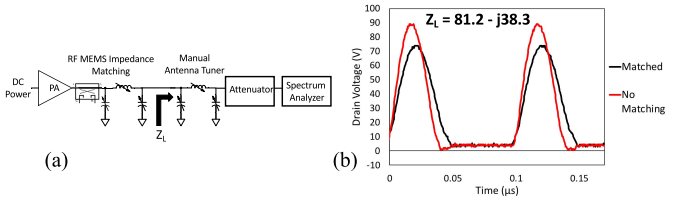

Fig. 10. Class-E power amplifier with (a) manual antenna tuner presenting a complex load impedance and (b) resulting voltage across the drain of the power amplifier FET with and without the RF MEMS impedance matching network.

as shown in Fig. 8, and the MEMS R_{on} and C_{off}. For the largest capacitor values, the parasitic ON-resistance of the switch can significantly degrade the transformation Q. Future versions of the matching network could parallel multiple MEMS switches to mitigate this effect, at the cost of somewhat increased layout complexity.

To improve the overall system efficiency, the matching network should present 50 Ω to the power amplifier and minimize insertion loss in the matching network itself. Fig. 10 shows an example of the MEMS matching network improving the power amplifier efficiency by maintaining the zero-voltage switching across the power amplifier FET when the unmatched load impedance is far from 50 Ω. Fig. 9(b) shows the calculated efficiency of the matching network over the range of S11 values that can be matched to 50 Ω. In some regions, the efficiency can be very low, especially on the outer edges of the smith chart, where most of the power is absorbed in the matching network itself instead. Consequently, we limit the matching network to a subset range, shown in Fig. 9(c), which eliminates all switch combinations that would lead to less than 80% matching network efficiency.

Further improvement of matching network efficiency can be achieved by additional limitations on S11 range. Ultimately, the matching network could be simplified using fewer inductor and capacitor values to minimize parasitic loss. However, the RF MEMs matching network provides flexible use with different coil geometries and positions within the MRI bore, since the WPT system must coexist with multiple types of anatomical MRI receive arrays. In future work, different WPT coil sizes may further reduce coupling to the MRI coils, and alternate flexible secondary coil designs may be explored for ultimate compatibility with flexible MRI receive coil arrays. Once the limitations on the coil geometry and coupled impedances are fully defined, the matching network could be optimized to minimize loss. Alternatively, the network could be removed altogether, as recent work [24], [25] has shown that if the coil geometry can be fixed, providing a constant coupling coefficient, then the power amplifier and rectifier can also be optimized and made independent of resistive changes to the load resistance on the rectifier.

The full system diagram, with the addition of the switched impedance matching network, is shown in Fig. 11. A dual switchable voltage power supply provides a low-power initial tune mode to protect the amplifier, and then a higher voltage for high-power tuning and operation. A passive nonferrous *LC* bandpass filter (BPF) provides additional harmonic attenuation after the power amplifier. Following the filter, a Bruene

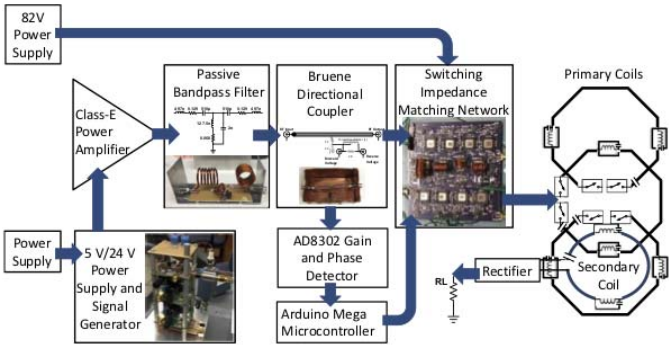

Fig. 11. Full system diagram with the class-E power amplifier and impedance matching system. The impedance mismatch is measured by a directional coupler and a gain and phase detector, then an Arduino microcontroller determines and switches in the optimal values.

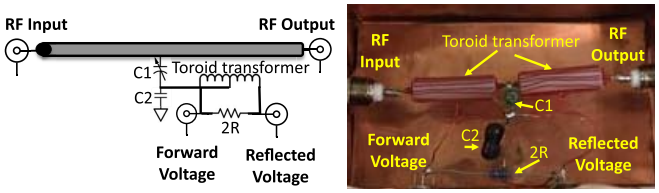

Fig. 12. Bruene directional coupler schematic and circuit constructed with discrete components and air-core toroids.

directional coupler, constructed with air-core toroids, shown in Fig. 12, samples the forward and reflected voltages. These signals serve as inputs to an AD8302 gain and phase detector to find the magnitude and the phase of the reflection coefficient, S11. S11 is then compared to a lookup table of all possible reflection coefficients, stored on an SD card of an Arduino Mega and Arduino Ethernet shield, which can be matched efficiently to 50 Ω. To account for errors in the phase measurement from the AD8302 and to prevent excessive insertion loss in the matching network, the tuning algorithm then sweeps through all switch combinations near the initial match but having a matching network efficiency above 80%. The switch combination that results in the lowest measured reflection coefficient magnitude is selected.

F. Class-E Rectifier

Hard-switching rectifier topologies, such as the full-bridge, generate high harmonic content at the input of the rectifier, reducing efficiency and causing interference in the MRI environment. Instead, different soft-switching-based class-E rectifiers, shown in Fig. 13, were compared to minimize harmonic back-emission that can cause MRI image degradation. A class-E rectifier was designed based on the analysis presented in [26], with the WPT coil modeled as a current source input. For $R_{L,\text{min}}$ of 4 Ω, L_r is about 200 nH and C_r is about 1.26 nF, which includes the parasitic capacitance of a B540C Schottky diode.

Half-wave rectifiers, such as the class-E rectifier, generally have higher harmonic voltage/current content at the input of the rectifiers as a result of their asymmetric waveforms. Alternatively, full-wave class-E rectifiers should create a near sinusoidal input waveform, resulting in lower harmonic generation [27]. The full-wave rectifier, shown in Fig. 13(b), is based on the equations in [28] for $R_{L,\text{min}}$ of 4 Ω and a duty cycle

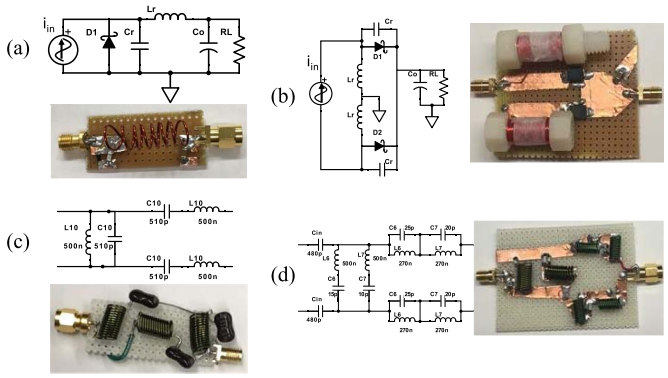

Fig. 13. Circuit schematic and physical implementation of the rectifier stage. (a) Class-E rectifier. (b) Full-wave class-E rectifier. (c) 10-MHz BPFs. (d) 60- and 70-MHz notch filters.

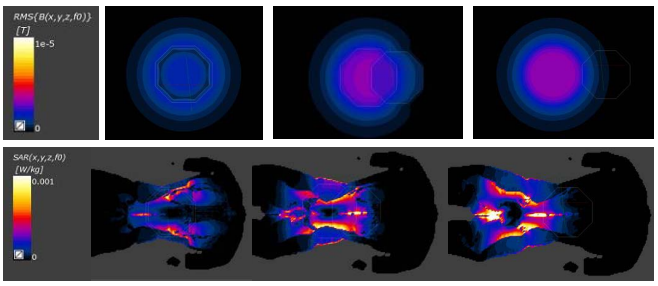

Fig. 14. SAR simulation results showing the B-field of the WPT coils (top) and SAR absorption of the body model as the secondary coil is moved from coaxial alignment to halfway and full diameter lateral shift (bottom).

of D = 0.49. The two L_r inductors should provide a large inductance with a low parasitic resistance to provide a low-loss return path for the dc current. For MRI compatibility, we required air-core inductors, which are physically large [Fig. 13(b)], with an inductance of about 5.8 μH.

Additional harmonic filters can be added at the input of the rectifier to minimize the back-emission of spurs near the MRI frequency. Fig. 13(c) shows a 10-MHz BPF designed to attenuate all high-frequency harmonics. Alternatively, Fig. 13(d) shows notch filters at 60 and 70 MHz to specifically target the highest harmonics near the MRI band (63.9 MHz for 1.5 Tesla), while an additional series capacitor is used to tune out any reactance these filters add at 10 MHz.

IV. SAR Simulations

To ensure the safety of our proposed prototype, we analyzed the tissue heating incurred by the combined set of power harvesting coils. A realistic body model [29] was inserted into the electromagnetic simulation package Sim4Life [30] using hexagonal loops for the primary and secondary coil elements with diameters of 20 and 18 cm, respectively. The simulation coil dimensions match the experimental system and are shown in Fig. 14. The vertical distance between the coils was 3.5 cm, and the coil pair was separated from the body model by 1 cm. The setup was analyzed at a sinusoidal frequency of 10 MHz. Coil positions were shifted from a coaxial arrangement to a quarter, halfway, three-quarter, and full diameter lateral shift.

As a first step, three magnetostatic simulations (1 A_{rms} excitation on primary coil only, on secondary coil only, and on both coils) determined the self-inductances of primary and secondary coils as well as the mutual inductance between the coils, by extracting an equivalent T-network of the structure. The load impedance of 4 Ω then yielded the induced current in the secondary coil. The second simulation step determined the B-field of the coupled structure using a magnetostatic analysis with a 1 A_{rms} excitation on the primary coil and the calculated induced current on the secondary coil. This B-field acted as the source vector field for a quasi-static simulation, in which E-fields and SAR levels could be determined.

Unit current excitation resulted in 0.25 W into the load. Results showed that the worst case peak spatial average SAR was found to be 0.07 W/kg (averaged over 1 g of tissue [31]), and 0.02 W/kg (averaged over 10 g of tissue [32], [33] for a 1 A_{rms} excitation. If scaled by 4× in current or 16× in power, these values could approach respective limits of 1.6 and 2.0 W/kg. The worst case mass averaged SAR over the entire body was 3.6×10^{-4} W/kg which, with similar scaling, would only reach 6 mW/kg. Peak spatial SAR was higher when coils were located in almost adjacent positions because of a lack of current cancelation and local superposition of coil E-fields. We conclude that the overall SAR footprint of the WPT prototype is small compared to standard MRI exam levels, which typically range from 0.5 to 2 W/kg averaged over the entire anatomy. A later human loading test, showing only 2%–3% efficiency drop, appears to validate this assertion.

V. Results and Discussion

A. System Efficiency

Bench-top efficiency tests were accomplished using a 24-V V_{DD} supply to the power amplifier, measuring RF output power with a spectrum analyzer via a 30-dB attenuator and dc output power with a multimeter. Efficiency was calculated by taking Pout/Pin, in which dc power Pin to the power amplifier was measured with a voltmeter and ammeter. For RF output power tests to 50 Ω, Pout was simply converted from dBm on the spectrum analyzer. For dc output power, the output voltage across the load resistor was measured with a multimeter and Pout was calculated from V^2/R. The $\eta_{\text{dc-RF}}$ efficiency of the power amplifier, when connected to a 50 Ω load, was 95.0% while delivering 24.4 W. With the addition of the matching network connected to a 50-Ω load, system efficiency dropped to 86.4% due to the losses through the matching network components.

The complete dc to dc system efficiency, η_{system}, was measured with a 3.5 cm separation between the WPT coils and a 4-Ω resistor load on the rectifier. Results for a variety of test conditions are tabulated in Table I. With the half-wave class-E rectifier but no BPF after the power amplifier, η_{system} was almost 63%. With the addition of the BPF, η_{system} dropped to 55% due to the additional parasitic losses through the filter components.

With a person laying on top of the WPT coils as would occur in the MRI environment, there is a slight decrease in efficiency of 2%–3%, likely due to the patient loading the coils, but it is not a significant loss. Inductively coupled conductive loss from the patient can be modeled as an additional parasitic resistance in the coils that increase quadratically with frequency [34]. Tissue conductivity of 0.5 S/m at 10 MHz, with

TABLE I
BENCHTOP SYSTEM EFFICIENCY

Rectifier		dc Input Power	Output Power	Efficiency
Class-E		21.564 W	13.58 W	62.97%
Class-E	With TX Side BPF	18.075 W	9.954 W	55.07%
Class-E	With Patient on Coils	15.94 W	8.352 W	52.39%
Class-E	With 10 MHz Filters	30.072 W	12.821 W	42.63%
Class-E	With 60/70 MHz Filters	30.506 W	11.955 W	39.19%
Full-Wave Class-E		24.267 W	10.181 W	41.95%
Full-Wave Class-E	With 10 MHz Filters	21.059 W	9.067 W	43.05%
Full-Wave Class-E	With 60/70 MHz Filters	26.036 W	8.58 W	32.95%

no separation between the patient and secondary coil, would induce at most an additional 0.75 Ω on the secondary coil and 0.71 Ω on the primary coil (3.5 cm away). A new maximum link efficiency ($\eta_{\text{link,max}}$) of 73.4% (a 12.9% reduction) would result. However, these equations assume an infinite conductive medium that, due to the size of our coils, overestimates the loss.

The full-wave class-E rectifier decreases the overall system efficiency to around 42%. Although the full-wave design can theoretically improve the rectifier efficiency by reducing harmonic components, the added parasitic resistances of the inductors in the dc return path contribute directly to power loss, and in the case where we have such a small (4 Ω) resistor load, this can become a significant source of loss. With both rectifiers, there is some efficiency loss with the addition of an input filter, and in both cases, the 60-/70-MHz notch filters result in a slightly higher efficiency loss. However, the worst case efficiency is still above 30% while delivering 8.6 W.

B. Spectral Noise and Harmonics

To assess the spectral harmonic and noise mixing with rectification, we observed the RF spectrum at the output of a battery-powered MRI preamplifier connected to a loaded MRI receive coil, as shown in Fig. 15. The loaded MRI coil was 5 cm above a deactivated (MEMs off) WPT primary element, while an adjacent (MEMs on) primary coil transmitted power to the WPT secondary coil. Fig. 15(c) shows that without a rectifier on the WPT secondary coil, there is little noise injection into the MRI coil when RF power is being delivered to the load resistor. Noise around the 10-MHz harmonics is shown to be significantly improved by adding the extra passive BPF at the class-E amplifier output.

With the addition of a nonlinear rectification element on the secondary coil, the harmonics around the MRI frequency increased by over 50 dB when the WPT system delivered 8 W of dc power and there is significant spectral growth around the 60-MHz harmonic. The half-wave class-E rectifier generated higher harmonics than the full-wave class-E, especially at the 50- and 70-MHz harmonics. However, both rectifiers upconverted significant RF noise into the MRI frequency band.

The noise conversion of either rectifier can be reduced by the addition of the bandpass or notch filters shown in Fig. 13 between the secondary coil and the rectifier input. For both rectifiers, the 60-/70-MHz notch filters reduced the 60-MHz harmonic by almost 10 dB more than the 10-MHz BPFs. The 60-/70-MHz notch filters also had the lowest spectral growth around the 60-MHz harmonic.

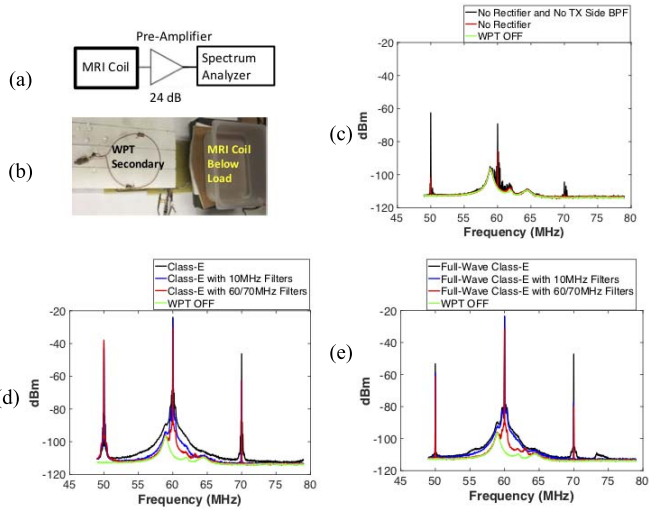

Fig. 15. Spectral interference caused by the WPT system delivering around 8-W–4-Ω resistor load. (a) and (b) Measurement setup with a loaded MRI surface receives coil connected to an MRI preamplifier and spectrum analyzer. (c) Noise spectrum with no rectifier and option of extra amplifier bandpass filtering. Only RF power is delivered to a load resistor. (d) Spectral interference with the half-wave class-E rectifier on the secondary coil with and without additional rectifier-side filtering. (e) Spectral interference with the full-wave class-E rectifier on the secondary coil with and without additional rectifier-side filtering.

From time-domain observations of the preamplifier output voltage, the harmonic generation was insufficient for any rectifier/filter combination to cause the preamplifier output to clip. For the full-wave class-E rectifier, the addition of the 60-/70-MHz notch filters dropped the peak-to-peak output voltage from about 200 to 70 mV. Although these peak-to-peak voltages did not saturate the preamplifier if the MRI and WPT coils were offset laterally, they could do so if coaxial. Moreover, even an unsaturated preamp of sufficient output amplitude could cause subsequent gain stages in the MRI receive chain to become saturated and block the MRI signal detection.

C. MR Imaging

To demonstrate WPT influences on MR image quality, 1.5 T images were acquired using MRI body coil transmit at 63.9 MHz and a 5-in (127 mm) receive surface coil. A gradient recalled echo (GRE) sequence acquired data using 24-cm FOV, 6-mm slice, a TR of 150 ms, and a TE of 15 ms. Tests were performed for continuous WPT, and with gated WPT in which the power transfer was disabled in a 13-ms window around data acquisition in the MRI pulse sequence.

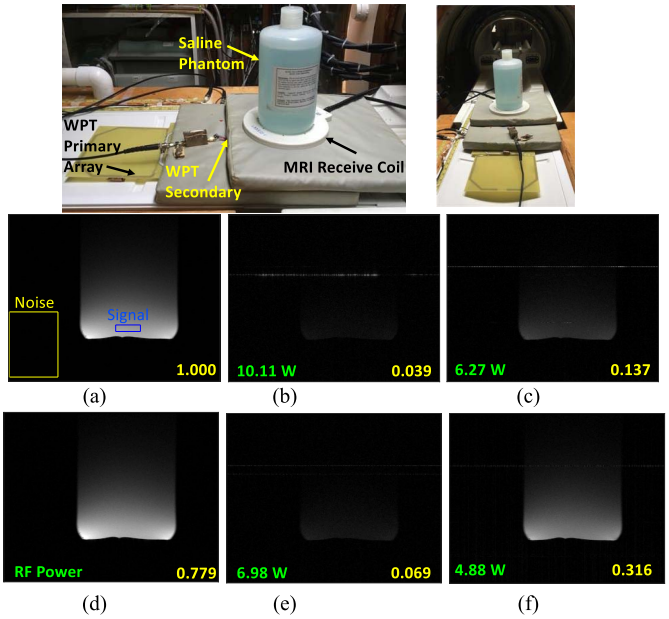

Fig. 16. Image results for high-power WPT. Received power and relative SNR are annotated for each image. Setup with WPT coils centered underneath the MRI receives coil and phantom (top). (a) Reference SNR image with the WPT system completely off. WPT system on with (b) unfiltered half-wave class-E rectifier, (c) half-wave class-E plus 60-/70-MHz notch filters, (d) unrectified RF power delivery, (e) unfiltered full-wave class-E rectifier, and (f) 60-/70-MHz notch filtered full-wave class-E rectifier.

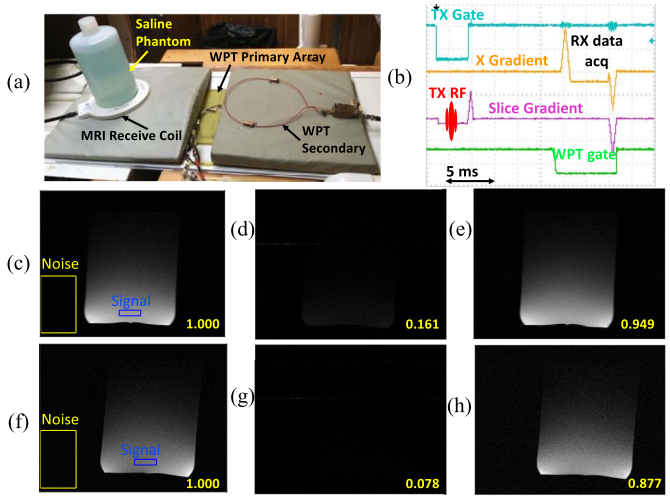

Fig. 17. (a) Test setup with the MRI receive coil and phantom moved laterally from the WPT secondary coil. (b) RF gating signal triggered by the TX exciter unblank signal and adjusted to match the MRI receive window. Image results and relative SNR with the half-wave class-E rectifier and a 4-Ω resistor on the WPT secondary coil receiving around 4.55 W when (c) WPT system is completely off, (d) continuously delivering power, and (e) gated RF power delivery. The MRI receive coil and phantom were then moved directly on top of the WPT secondary coil and imaging was repeated for (f) WPT system completely off (g) continuous power delivery, and (h) gated RF power delivery.

The physical test setup is shown in Fig. 16. The WPT primary and secondary coils are centered underneath an MRI receive coil and phantom, resulting in a high likelihood of coupling between the WPT coils and the MRI coil due to their proximity. The annotated relative SNR of each image was calculated using the outlined signal and noise regions for comparison with a reference image (normalized to relative SNR=1) taken with the WPT system off.

For all tests, the power amplifier included the auxiliary postfilter. Initially, very low power (200–500 mW) tests were performed for half- and full-wave rectifiers with no harmonic filter, 60-/70-MHz notch filter or 10-MHz bandpass. As with the spectral tests, the 10-MHz bandpass SNR underperformed the notch filter SNR by 50% (half-wave rectifier) but only by 6% for the full-wave rectifier. Consequently, for continuous high-power WPT tests, only the notch filter configuration was used in subsequent rectifier imaging tests.

Fig. 16 shows the image results when transmitting and receiving higher power. Once again, both the full-wave class-E rectifier and 60-/70-MHz notch filters significantly improved the image SNR compared to the half-wave class-E rectifier without filters, but at the cost of reduced WPT system efficiency. SNR was also significantly higher when the rectifier was removed entirely and only RF power was delivered by the WPT secondary coil to a 4-Ω resistor load. With the best case combination of the 60-/70-MHz filters at the full-wave class-E rectifier input, the MRI preamplifier is not being blocked by the WPT system and the image looks reasonable; however, the SNR is still significantly lower than the reference image. This could be further improved by additional filtering on the dc supply lines entering the MRI scan room or by restricting how close the MRI receive coil is to WPT system. The 5-in (127 mm) MRI receive surface coil is similar in size to the WPT secondary and centered over the WPT system, so any offset or increase in distance from the WPT system should improve SNR. In addition, a practical MRI receive array would use smaller diameter coils that would further decrease coupling to the WPT system. With continuous WPT, harmonic rectifier filters are essential to improve SNR. Although the results are converging to the reference SNR, full SNR recovery still requires filter improvements.

The alternative approach is simply to gate the WPT system off in the readout interval within the MRI pulse sequence where data are actually digitized. Fig. 17(b) shows a 13-ms gating interval surrounding the data acquisition. TR was again 150 ms for a GRE sequence. Two image sets are shown using a half-wave class-E rectifier and no filters: Fig. (c)–(e) with the MRI coil offset from the WPT loops, and then Fig. 17(f)–(h) where MRI coil and phantom are above the WPT secondary. The gated image of Fig. 17(e) and (h) is about 1 dB within the reference SNR of Fig. 17(c) and (f) (obtained with WPT systems all off), while the ungated images, Fig. 17(d) and (g) demonstrates the role of proximity in SNR degradation.

VI. Conclusion

This paper presents a complete WPT prototype designed to deliver several watts of power inside the MRI environment with the goal of developing completely wireless MRI patient coils. WPT coils must be collocated with the MRI receive coils while maintaining the MRI image SNR. The limiting noise floor of MRI is the thermal noise of the body, resulting in very strict requirements for an MRI compatible WPT system. This MRI WPT system includes a high-efficiency class-E

power amplifier, an automated RF-MEMs impedance matching network, an array of primary coils with RF MEMs control, and a single flexible secondary coil. Using a resonant class-E rectifier, this system demonstrated more than 10-W power delivery with high efficiency at several centimeters of coil separation. However, the addition of the nonlinear rectification element significantly degrades the MR image quality in continuous power transfer if harmonic filters are absent.

Efficiency can be traded for additional filtering and full-wave class-E rectification that naturally generates lower power harmonics. However, at 5-W WPT levels, filtering still does not achieve the full thermal noise limited SNR of MRI. Instead, gated WPT, in which power transfer is interrupted during the MRI signal acquisition window, does allow SNR performance to approach within 1 dB of the ideal. Future work will include imaging with MRI receive arrays of differing dimensions and in different locations relative to the WPT coils, as well as further filtering efforts to converge on the MRI SNR limit with continuous WPT. Finally, work remains to determine if the WPT signal phase stability is sufficient to provide a synchronous sampling clock in a wearable MRI array. For the present system, the feasibility of WPT within an MRI scanner has been fully demonstrated.

ACKNOWLEDGMENT

The authors would like to thank T. Grafendorfer of GE Healthcare for research support. The authors would also like to thank M. Seth and C. Giovanniello of Menlo Micro for the RF MEMs support.

REFERENCES

[1] C. J. Hardy *et al.*, "128-channel body MRI with a flexible high-density receiver-coil array," *J. Magn. Reson. Imag.*, vol. 28, no. 5, pp. 1219–1225, Nov. 2008.

[2] J. R. Corea, P. B. Lechene, M. Lustig, and A. C. Arias, "Materials and methods for higher performance screen-printed flexible MRI receive coils," *Magn. Reson. Med.*, vol. 78, no. 2, pp. 775–783, Aug. 2016.

[3] S. Vasanawala *et al.* (2017). "Development and clinical implementation of next generation very light weight and extremely flexible receiver arrays for pediatric MRI." [Online]. Available: https://arxiv.org/abs/1705.00224

[4] K. Byron, F. Robb, S. Vasanawala, J. Pauly, and G. Scott, "A wireless power transfer system for mri scanners," in *Proc. IEEE WPTC*, Jun. 2018, pp. 1–4.

[5] J. Garnica, R. A. Chinga, and J. Lin, "Wireless power transmission: From far field to near field," *Proc. IEEE*, vol. 101, no. 6, pp. 1321–1331, Jun. 2013.

[6] B. Lenaerts and R. Puers, *Omnidirectional Inductive Powering for Biomedical Implants*. Dordrecht, The Netherlands: Springer, 2009.

[7] R. W. P. King, *Fundamentals of Electromagnetic Theory*. New York, NY, USA: Dover, 1963.

[8] K. Byron, F. Robb, P. Stang, S. Vasanawala, J. Pauly, and G. Scott, "An RF-gated wireless power transfer system for wireless MRI receive arrays," *Concepts Magn. Reson. B, Magn. Reson. Eng.*, vol. 47B, no. 4, Oct. 2017, Art. no. e21360. doi: 10.1002/cmr.b.21360

[9] P. B. Roemer, W. A. Edelstein, C. E. Hayes, S. P. Souza, and O. M. Mueller, "The NMR phased array," *Magn. Reson. Med.*, vol. 16, no. 2, pp. 192–225, 1990.

[10] W. Chen, R. A. Chinga, S. Yoshida, J. Lin, C. Chen, and W. Lo, "A 25.6 W 13.56 MHz wireless power transfer system with a 94% efficiency GaN class-E power amplifier," in *IEEE MTT-S Int. Microw. Symp. Dig.*, Jun. 2012, pp. 1–3.

[11] J. J. Casanova, Z. N. Low, and J. Lin, "Design and optimization of a class-E amplifier for a loosely coupled planar wireless power system," *IEEE Trans. Circuits Syst., II, Exp. Briefs*, vol. 56, no. 11, pp. 830–834, 2009.

[12] M. Pinuela, D. C. Yates, S. Lucyszyn, and P. D. Mitcheson, "Maximizing DC-to-load efficiency for inductive power transfer," *IEEE Trans. Power Electron.*, vol. 28, no. 5, pp. 2437–2447, May 2013.

[13] J.-R. Yang, J. Kim, and Y.-J. Park, "Class E power amplifiers using high-Q inductors for loosely coupled wireless power transfer system," *J. Elect. Eng. Technol.*, vol. 9, no. 2, pp. 569–575, Mar. 2014.

[14] A. Grebennikov, N. O. Sokal, and M. J. Franco, *Switchmode RF and Microwave Power Amplifiers*. New York, NY, USA: Academic, 2012.

[15] N. O. Sokal and A. D. Sokal, "Class E-A new class of high-efficiency tuned single-ended switching power amplifiers," *IEEE J. Solid-State Circuits*, vol. 10, no. 3, pp. 168–176, Jun. 1975.

[16] M. K. Kazimierczuk and K. Puczko, "Exact analysis of class E tuned power amplifier at any Q and switch duty cycle," *IEEE Trans. Circuits Syst.*, vol. 34, no. 2, pp. 149–159, Feb. 1987.

[17] N. O. Sokal, "Class-E RF power amplifiers," *QEX Commun. Quart.*, vol. 204, pp. 9–20, Jan. 2001.

[18] A. Lidow and M. De Rooij, "Performance evaluation of enhancement-mode GaN transistors in class-D and class-E wireless power transfer systems," *Bodo Mag.*, vol. 64717, pp. 56–60, May 2014.

[19] J. Choi, D. Tsukiyama, and J. Rivas, "Comparison of SiC and eGaN devices in a 6.78 MHz 2.2 kW resonant inverter for wireless power transfer," in *Proc. IEEE Energy Convers. Congr. Expo. (ECCE)*, Sep. 2016, pp. 1–6.

[20] M. de Rooij, "Performance comparison for A4WP class-3 wireless power compliance between eGaN FET and MOSFET in a ZVS class D amplifier," in *Proc. PCIM*, May 2015, pp. 1–8.

[21] Y. Lim, H. Tang, S. Lim, and J. Park, "An adaptive impedance-matching network based on a novel capacitor matrix for wireless power transfer," *IEEE Trans. Power Electron.*, vol. 29, no. 8, pp. 4403–4413, Aug. 2014.

[22] S. B. Bulumulla, K. J. Park, E. Fiveland, J. Iannotti, and F. Robb, "MEMS switch integrated radio frequency coils and arrays for magnetic resonance imaging," *Rev. Sci. Instrum.*, vol. 88, no. 2, Feb. 2017, Art. no. 025003.

[23] D. Spence and M. Aimi, "Custom MEMS switch for mr surface coil decoupling," in *Proc. 23rd Annu. Meeting ISMRM*, vol. 23, 2015, p. 704.

[24] A. Pacini, A. Costanzo, S. Aldhaher, and P. D. Mitcheson, "Load- and position-independent moving MHz WPT system based on GaN-distributed current sources," *IEEE Trans. Microw. Theory Techn.*, vol. 65, no. 12, pp. 5367–5376, Dec. 2017.

[25] T. Nagashima *et al.*, "Analytical design procedure for resonant inductively coupled wireless power transfer system with class-E^2DC-DC converter," in *Proc. IEEE Int. Symp. Circuits Syst. (ISCAS)*, Jun. 2014, pp. 113–116.

[26] M. K. Kazimierczuk, "Analysis of class E zero-voltage-switching rectifier," *IEEE Trans. Circuits Syst.*, vol. 37, no. 6, pp. 747–755, Jun. 1990.

[27] A. Reatti, M. Kazimierczuk, and R. Redl, "Class E full-wave low dv/dt rectifier," *IEEE Trans. Circuits Syst. I, Fundam. Theory Appl.*, vol. 40, no. 2, pp. 73–85, Feb. 1993.

[28] M. Liu, M. Fu, and C. Ma, "Low-harmonic-contents and high-efficiency class E full-wave current-driven rectifier for megahertz wireless power transfer systems," *IEEE Trans. Power Electron.*, vol. 32, no. 2, pp. 1198–1209, Feb. 2017.

[29] A. Christ et al, "The virtual family–development of surface-based anatomical models of two adults and two children for dosimetric simulations," *Phys. Med. Biol.*, vol. 55, no. 2, pp. N23–38, Jan. 2009.

[30] Z. MedTech. *Sim4life*. Accessed: May 2018. [Online]. Available: https://zmt.swiss/sim4life

[31] *Radio Frequency Safety*. Accessed: Oct. 2, 2017. [Online]. Available: https://www.fcc.gov/general/radio-frequency-safety-0

[32] *IEEE Standard for Safety Levels with Respect to Human Exposure to Radio Frequency Electromagnetic Fields, 3 khz to 300 ghz*, Standard IEEE C95. 1-1991, I. S. C. Committee, 1992.

[33] A. Ahlbom et al, "Guidelines for limiting exposure to time-varying electric, magnetic, and electromagnetic fields (up to 300 GHz)," *Health Phys.*, vol. 75, no. 4, pp. 494–521, Apr. 1998.

[34] B. H. Suits, A. N. Garroway, and J. B. Miller, "Surface and gradiometer coils near a conducting body: The lift-off effect," *J. Magn. Reson.*, vol. 135, no. 2, pp. 373–379, Dec. 1998.

Authors' photographs and biographies not available at the time of publication.